

Unleashing Diffusion and State Space Models for Medical Image Segmentation

Rong Wu^a, Ziqi Chen^b, Liming Zhong^c, Heng Li^d, Hai Shu^{a,*}

^aDepartment of Biostatistics, School of Global Public Health, New York University, New York, NY, USA

^bSchool of Statistics, KLATASDS-MOE, East China Normal University, Shanghai, China,

^cSchool of Biomedical Engineering, Southern Medical University, Guangzhou, China,

^dFaculty of Biomedical Engineering, Shenzhen University of Advanced Technology, Guangzhou, China,

Abstract

Existing segmentation models trained on a single medical imaging dataset often lack robustness when encountering unseen organs or tumors. Developing a robust model capable of identifying rare or novel tumor categories not present during training is crucial for advancing medical imaging applications. We propose DSM, a novel framework that leverages diffusion and state space models to segment unseen tumor categories beyond the training data. DSM utilizes two sets of object queries trained within modified attention decoders to enhance classification accuracy. Initially, the model learns organ queries using an object-aware feature grouping strategy to capture organ-level visual features. It then refines tumor queries by focusing on diffusion-based visual prompts, enabling precise segmentation of previously unseen tumors. Furthermore, we incorporate diffusion-guided feature fusion to improve semantic segmentation performance. By integrating CLIP text embeddings, DSM captures category-sensitive classes to improve linguistic transfer knowledge, thereby enhancing the model’s robustness across diverse scenarios and multi-label tasks. Extensive experiments demonstrate the superior performance of DSM in various tumor segmentation tasks. Code is available at <https://github.com/Rows21/KMax-Mamba>.

Keywords: Diffusion process, State space model, Text embeddings, Medical image segmentation

1. Introduction

A significant challenge in medical image segmentation lies in adapting a model to diverse segmentation tasks, particularly those involving rare diseases [1]. Most existing models, trained on a single medical imaging dataset, lack reliability and robustness when applied to different organs or tumors. Recent studies [2, 3] have aimed to develop a unified model capable of addressing a broad spectrum of organs and tumors. However, these models often struggle with blurred edge detection in multi-class object detection and segmentation tasks, and continue to face difficulties in identifying clinically relevant rare or novel lesion classes. For many types of cancer, the ability to accurately detect and segment tumors is critical, directly impacting treatment decisions and cancer prognosis. In such scenarios, there is a strong demand for a medical image segmentation model that can effectively identify rare diseases with limited instances and precisely segment tumor lesions. In this study, we integrate Diffusion Models, State Space Models (SSMs), and Open-Vocabulary Semantic Segmentation (OVSS) to further enhance performance across various tumor segmentation tasks.

SSMs [4, 5] have emerged as a prominent topic in the fields of computer vision and language modeling. To address the challenges associated with long sequence modeling, Mamba [5], derived from the foundational SSM framework [6], offers a

solution designed to capture extensive dependencies and enhance training efficiency via a selection mechanism. Numerous studies have explored the application of Mamba across various imaging tasks. U-Mamba [7] integrates the Mamba layer into the encoder of nnUNet [8] to boost general medical image segmentation capabilities. Vision Mamba [9] introduces a bidirectional SSM for data-driven global visual context modeling and incorporates position embeddings for spatially informed visual comprehension. Mamba-2 [10] highlights the significant performance gains achieved by effectively integrating the Transformer module [11] with SSM within the network. Nonetheless, the fusion of Transformer and SSM remains underexplored, particularly in the domain of medical image segmentation tasks.

Diffusion models [12, 13] have recently garnered significant attention for their utility in addressing medical imaging challenges. A key advantage of diffusion models is their ability to generate high-quality samples comparable to those produced by Generative Adversarial Networks (GANs), while demonstrating superior robustness against mode collapse [13, 14]. Initially, diffusion models were developed to augment datasets and harmonize sample distributions. However, recent studies have highlighted their effectiveness in addressing issues related to visual boundary enhancement in imaging tasks [15, 16].

OVSS methods [17, 18], incorporating vision-language models (VLMs) like CLIP [19], have found diverse applications within the broader image processing domain. This methodology facilitates the transfer of knowledge from fixed categories to unknown (novel) ones by learning transferable rep-

*Corresponding author: hs120@nyu.edu

representations from the annotated data of known classes to represent unknown ones [20, 21]. Leveraging the robust zero-shot transfer capabilities demonstrated by CLIP, researchers have been actively developing advanced open-vocabulary models by harnessing extensive image-text pairs for detailed vision tasks in detection [2, 22] and segmentation [23, 24]. Some strategies integrate object queries from MaskFormer [25, 26] models, trained on base categories, to produce class-agnostic mask proposals. These proposals are subsequently classified using vision-language models, showcasing remarkable and resilient zero-shot segmentation prowess.

In the realm of medical imaging, the development of a unified model holds the potential to streamline data integration by amalgamating information from various medical institutions. This amalgamation allows the model to acquire knowledge from a broader spectrum of data, thereby enhancing its adaptability and learning capacity. In clinical settings, the use of unified models eliminates the need for technicians to switch between multiple models while handling various tasks. Nevertheless, these models require substantial amounts of labeled data and face challenges in identifying rare or novel lesion categories that are clinically important.

To tackle these challenges, we introduce a novel framework, **Diffusion and State Spaces Model (DSM)**, designed to: (1) enhance semantic segmentation between organs and tumors, and (2) boost the robustness of multi-organ recognition capabilities. Our DSM involves setting up two types of queries—organ queries and tumor queries—to represent distinct embeddings. The organ queries are trained during a preliminary stage. Subsequently, DSM integrates multi-scale feature maps with diffusion-guided refinement maps to improve tumor boundary detection. Following this, DSM creates mask prompts for out-of-distribution regions within organs to help accurately identify tumor features. The refined mask features and mask prompts are then fed into Transformer decoders to detect tumor region, facilitating accurate segmentation and recognition tasks.

Our main contributions are summarized as follows:

- DSM incorporates a novel kMax-Mamba layer, a key innovation designed to enhance the model’s ability to retain and utilize long-term memory for query embeddings. By effectively modeling long-range dependencies, the kMax-Mamba layer ensures that crucial information is preserved during the processing of query embeddings, leading to more accurate and robust predictions.
- DSM addresses the challenge of distinguishing between tumor and organ regions by introducing a mask prompt after the vision decoder. This prompt prioritizes the detection of tumor features within organ regions by focusing on the model’s attention on out-of-distribution regions. This approach not only improves the model’s ability to detect and segment tumors but also ensures robustness across diverse datasets.
- DSM leverages a diffusion-guided query decoder to refine the segmentation process by focusing on the precise delin-

ation of tumor boundaries. This decoder integrates diffusion processes to smooth and enhance feature maps, enabling the capture of subtle variations in tumor boundaries and improving overall segmentation accuracy.

2. Related Work

2.1. Multi-Organ and Tumor Segmentation

Advancements in U-Net-based architectures [8, 27] and deep learning methodologies [28] have significantly propelled the field of multi-organ and tumor segmentation. Since the introduction of the Segment Anything Model (SAM) [29], the integration of subsequent transformer blocks into the network architecture backbone [30, 31] has been under investigation. Our study primarily delves into addressing early-stage tumor detection issues in medical image segmentation, where current solutions exhibit limited performance, particularly in multi-organ segmentation [2, 13]. Hence, we explore a novel architecture that combines Transformer [11] and Mamba [5] models to enhance segmentation performance in clinical scenarios, with emphasis on detecting and diagnosing minority tumors [32].

2.2. Open-Vocabulary Semantic Segmentation

The rapid progress in large-scale language models, such as GPT [33], BERT [20], and Med-PaLM [34], has significantly advanced natural language understanding and generation. These developments have inspired the emergence of large-scale pre-trained vision-language models (VLMs) that integrate visual and textual information for more generalizable and context-aware perception [35–37]. In particular, open-vocabulary semantic segmentation (OVSS), where models are tasked with segmenting arbitrary objects based on natural language descriptions rather than fixed class labels, has become a promising paradigm for addressing the limitations of closed-set segmentation systems.

2.3. Prompt-based Zero-shot Models

Recent work on large language models has explored in-context learning for medical image segmentation and can segment any class guided by example images or text [38, 39]. SAMMed [38] fine-tunes SAM on large 3D medical datasets using the bounding box but lacks the ability for detailed editing. UniverSeg [39] generalizes well across diverse medical imaging tasks and modalities by leveraging a unified architecture trained on multiple datasets with task-specific prompts. However, it struggles with unseen tumors whose associated organs or rare anatomical structures are not well represented in training data, and its performance depends heavily on the quality of prompt images.

2.4. Unseen Tumor Detection and Localization

Recent studies [40, 41] have proposed novel approaches for detecting or segmenting previously unseen tumors or lesions, often framing the task as a form of out-of-distribution (OOD)

detection. These methods aim to identify and localize anomalies that were not explicitly present in the training data, leveraging techniques such as distribution modeling or self-supervised representation learning. In the context of medical imaging, such unseen tumors often represent rare pathologies, subtle lesions, or atypical anatomical variations that deviate from the model’s learned distribution. It is essential to distinguish between traditional OOD detection and the zero-shot segmentation task explored in this paper. This distinction underlines the importance of open-vocabulary capabilities and cross-modal understanding in advancing the generalizability of segmentation models in medical imaging.

3. Preliminaries

3.1. State Space Models

SSMs are inspired by the continuous system that maps a 1-D function or sequence $x(t) \in \mathbb{R}$ to an output $y(t) \in \mathbb{R}$ through a hidden state $h(t) \in \mathbb{R}^N$. This system uses evolution parameter $\mathbf{A} \in \mathbb{R}^{N \times N}$, projection parameters $\mathbf{B} \in \mathbb{R}^{N \times 1}$ and $\mathbf{C} \in \mathbb{R}^{1 \times N}$, and can be represented as the following linear ordinary differential equation:

$$h'(t) = \mathbf{A}h(t) + \mathbf{B}x(t), \quad (1)$$

$$y(t) = \mathbf{C}h(t). \quad (2)$$

The Structured State Space sequence model (S4) [4] and Mamba [5] are discrete versions of this continuous system, which incorporate a step size Δ to approximate the continuous parameters $\{\mathbf{A}, \mathbf{B}\}$ into discrete approximations $\{\bar{\mathbf{A}}, \bar{\mathbf{B}}\}$. For example, Mamba uses the zero-order hold (ZOH) discretization rule:

$$\bar{\mathbf{A}} = \exp(\Delta\mathbf{A}), \quad (3)$$

$$\bar{\mathbf{B}} = (\Delta\mathbf{A})^{-1}(\exp(\Delta\mathbf{A}) - \mathbf{I})\Delta\mathbf{B}. \quad (4)$$

The discretized version of the system is then written as:

$$h_t = \bar{\mathbf{A}}h_{t-1} + \bar{\mathbf{B}}x_t, \quad (5)$$

$$y_t = \mathbf{C}h_t, \quad (6)$$

where $x_t = x(t\Delta)$ and $h_{-1} = 0$. Thus, the models can be computed via a global convolution.

3.2. Diffusion Process

Diffusion process [15, 42] is capable of learning a sequence of state transitions to generate high-quality samples from noise. Other than the generation capabilities derived from noise in diffusion models, we leverage the diffusion process in this work to improve visual boundary clarity, thereby enhancing segmentation performance. This process involves designing a diffusivity function D to solve a second-order partial differential equation. Given a feature map \mathbf{F} to be smoothed, the diffusion process is described as:

$$\frac{\partial \mathbf{F}}{\partial t} = \text{Div}(D(\mathbf{F}) \cdot \nabla \mathbf{F}), \quad (7)$$

where $\frac{\partial \mathbf{F}}{\partial t}$ is the time derivative of the solution matrix, ∇ is the gradient operator, Div is the divergence operator, and D is a diffusivity function depending on the input. As time t progresses, the solution \mathbf{F} gradually becomes smoother compared to the original matrix, as discussed in [15]. In numerous medical image segmentation scenarios, the blurring of class boundaries is a common concern. Our study aims to extract refined boundary features by employing linear diffusion processes that smooth both backgrounds and edges. This diffusion process applies more smoothing to regions parallel to boundaries than to regions perpendicular to these edges. Specifically, given a feature \mathbf{F} in areas with ambiguous boundaries, it undergoes a time-stepwise diffusion process. The intention is for the final state of the diffused feature to precisely delineate the boundaries between different anatomical structures.

4. Method

Our DSM framework operates in two stages: Stage 1 focuses on organ queries generation, and Stage 2 on tumor queries refinement. This section elaborates on both stages.

4.1. Stage 1: Organ Queries Generation

Our Stage 1 network structure is constructed based on MaskFormer [25, 26]. A vision encoder extracts pixel features using either a CNN [43] or a Transformer [44] backbone, while the vision decoder is responsible for reconstructing multi-scale feature maps $\{\mathbf{F}_i\}_{i=1}^4$, where $\mathbf{F}_i \in \mathbb{R}^{H_i \times W_i \times D_i \times C_i}$, with H_i , W_i , D_i , and C_i denoting the height, width, depth, and channel dimensions of feature maps for each decoder layer, respectively. Finally, the vision decoder within the backbone network progressively up-samples visual features into high-resolution image embedding $\hat{\mathbf{F}}_4 \in \mathbb{R}^{HWD \times C}$.

In Stage 1, a set of organ queries $\mathbf{O} \in \mathbb{R}^{N_o \times C}$ is randomly generated in the model, where N_o is the number of organ types. A kMax-Mamba (kMM) decoder K_d updates the queries by interacting with multi-scale visual feature maps $\{\mathbf{F}_i\}_{i=1}^4$. To capture organ-level information and tackle challenges related to long-tailed distributions, a proposed object-aware feature grouping strategy is implemented in K_d . Additionally, to enhance global context understanding in query features, a SSM layer is employed to maintain long-term knowledge in the kMM decoder. This approach guides each organ query to accurately represent and specify its corresponding organ category.

4.1.1. KMax-Mamba

As shown in Figure 1, K_d consists of a series of SSM and attention blocks that enable the queries to interact with multi-scale features. The traditional cross-attention layer updates the organ queries $\mathbf{O} \in \mathbb{R}^{N_o \times C}$ by

$$\hat{\mathbf{O}} = \mathbf{O} + \arg \max_{N_o} (\mathbf{Q}_O \mathbf{K}_F^T) \mathbf{V}_F, \quad (8)$$

where the superscripts O and F represent query and visual features, respectively. As shown in Figure 1, the $\arg \max$ on N_o

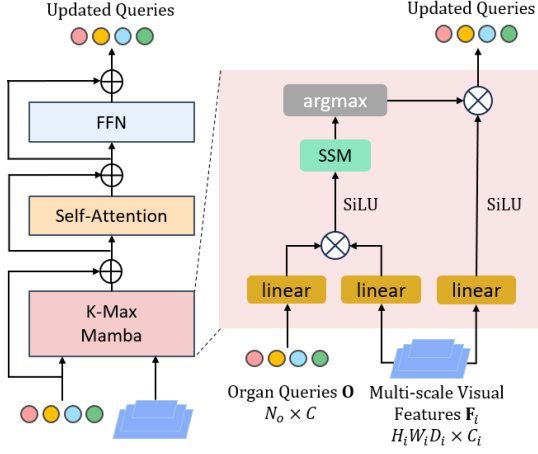


Figure 1: kMax-Mamba (kMM) structure: To convert a Transformer decoder into a kMM decoder, we add an SSM block after the cross-attention between queries and features.

acts as a query-wise grouping strategy as in k-means, attempting to group feature maps into query embedding. We leverage this query-wise argmax from kMax-deeplab [45] to replace spatial-wise softmax in the initial cross-attention settings, aligning visual features with queries and mitigating the issue of long-tail problems. Inspired by Mamba [4], we employ a SSM layer before arg max to maintain stable query embedding while training. In the i -th kMM block, the model leverages global information from multi-scale feature maps \mathbf{F}_i through a k-means SSM layer, implemented as below:

$$\mathbf{R}_i = \arg \max_{N_o} (\text{SSM}(\mathbf{O}_i \mathbf{F}_i^T)), \quad (9)$$

$$\hat{\mathbf{O}}_i = \mathbf{R}_i \mathbf{F}_i, \quad (10)$$

where $\mathbf{O}_i \in \mathbb{R}^{N_o \times C_i}$, $\mathbf{F}_i \in \mathbb{R}^{H_i W_i D_i \times C_i}$, and $\mathbf{R}_i \in \mathbb{R}^{N_o \times H_i W_i D_i}$ represent queries, feature maps, and query response, respectively. Query embedding $\hat{\mathbf{O}}_i$ is the linear projection from \mathbf{O} for each decoder layer. The features then go through SiLU activation function [46] and the SSM layer to maintain long-term knowledge memory. Finally, we adopt a cluster-wise argmax to update the organ queries as $\hat{\mathbf{O}}_i$ and go through a projection layer to obtain $\hat{\mathbf{O}} \in \mathbb{R}^{N_o \times C}$.

As depicted in Figure 2(a), after processing through the vision decoder and kMM decoder, we obtain updated organ queries $\hat{\mathbf{O}}$ and high-resolution image embeddings $\hat{\mathbf{F}}_4 \in \mathbb{R}^{HWD \times C}$. The semantic soft masks $\hat{\mathbf{Y}} \in [0, 1]^{N_o \times HWD}$ for organ queries are derived through a fixed match between the query embedding $\hat{\mathbf{O}}$ and high-resolution image features $\hat{\mathbf{F}}_4$, followed by a sigmoid function.

4.1.2. Loss Functions

We utilize the Dice loss to supervise the predicted soft masks overall and a Binary Cross-Entropy (BCE) loss to supervise the category information of organs after processing query embeddings through an MLP layer. Denote ground-truth one-hot labels $\mathbf{Y} = (Y_{ij})$ and soft masks $\hat{\mathbf{Y}} = (\hat{Y}_{ij})$, where $i = 1, \dots, N_o$ and

$j = 1, \dots, HWD$:

$$\mathcal{L}_{Dice} = \sum_{k=1}^K \sum_{j=1}^{HWD} \left[1 - \frac{2Y_{kj}\hat{Y}_{kj}}{Y_{kj} + \hat{Y}_{kj}} \right], \quad (11)$$

$$\mathcal{L}_{BCE} = - \sum_{k=1}^K \sum_{j=1}^{HWD} [Y_{kj} \log(\hat{Y}_{kj}) + (1 - Y_{kj}) \log(1 - \hat{Y}_{kj})], \quad (12)$$

$$\mathcal{L} = \mathcal{L}_{Dice} + \mathcal{L}_{BCE}, \quad (13)$$

where K ($K \leq N_o$) is the number of specified masked organ tasks for every image. Note that only the loss for masked organs is calculated during each iteration, which is called the partial labeled strategy [2]. This approach explicitly encourages well-defined boundaries between different categories, thereby reducing the risk of mixed representations where the target and surrounding regions might be clustered together.

4.2. Stage 2: Tumor Queries Refinement

After completing Stage 1, we generate a query response \mathbf{R}_4 , indicating the affinity between visual features and organ queries, along with updated organ queries that signify different organs. Moving on to Stage 2, our objective is to establish a new set of queries called tumor queries $\mathbf{T} \in \mathbb{R}^{N_T \times C}$ to detect and classify tumors, where N_T is the total number of tumor types. Note that N_T may not necessarily match that of organ queries N_o , as we aim to equip the model with zero-shot segmentation capabilities. The key idea here is to empower tumor queries to identify anomaly information indicative of tumors by leveraging organ queries, thereby enhancing the visual delineation of tumor boundaries.

We propose a novel approach to reframe tumor segmentation as a multi-prompting process, where the tumor queries not only recognize abnormal information associated with pathological changes but also discern the accurate boundaries between organs and tumors. To achieve this, we create mask visual prompts that enable the tumor queries to perceive abnormal information linked to pathological alterations in the features. Additionally, we implement a boundary enhancement strategy on multi-scale visual feature maps to facilitate easier detection of tumor textures. In Stage 1, we preserve the training datasets with organ labels to prevent the forgetting issue of the queries and introduce several datasets containing tumor labels for Stage 2. It is crucial to emphasize that the test phase encompasses novel tumor categories, validating the “zero-shot” nature of our method.

4.2.1. Anomaly Mask Visual Prompt

As depicted in Figure 2(b), the input image and queries undergo processing by the encoder, vision decoder, and kMM-decoder to acquire multi-scale visual features, high-resolution image embeddings, and refined organ queries, respectively. We then compute the maximum likelihood distribution embedding through the negative maximal process. In essence, the maximal query response from outliers typically yields smaller values compared to inliers. We use the negative maximal query

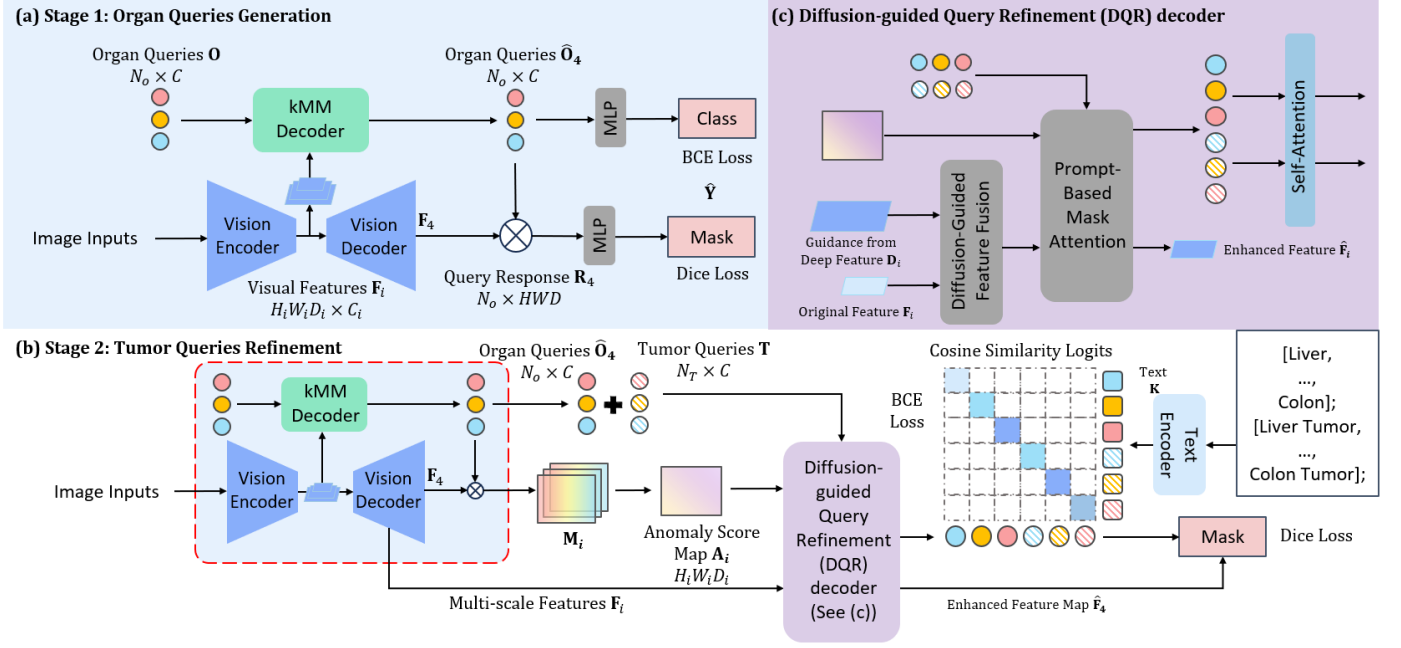


Figure 2: Pipeline overview: (a) Stage 1: Leveraging the kMax-Transformer, we introduce a feature grouping approach with SSM layers to train a series of organ queries for multi-organ segmentation. (b) Stage 2: We develop tumor queries for precise tumor segmentation by: (1) focusing on visual cues generated by OOD detection; (2) utilizing diffusion-guided boundary feature enhancement within a Transformer decoder. Finally, we integrate text embeddings with class queries to enhance the alignment, promoting cross-modal reasoning. (c) Specified explanation in Diffusion-guided Query Refinement (DQR) decoder: The multi-scale feature maps are first fused using a feature fusion strategy, then prompted with masks generated by OOD detection, and finally the refined organ and tumor queries are output.

response $\mathbf{R}_i \in \mathbb{R}^{N_o \times H_i W_i D_i}$ within the multi-scale mask prediction \mathbf{F}_i as the anomaly score map \mathbf{A}_i by

$$\mathbf{A}_i = -\max_{N_o} \mathbf{R}_i, \quad i = 1, \dots, 4. \quad (14)$$

We then normalize the anomaly score map into mask prompts \mathbf{M}_i using min-max normalization with a threshold of 0.5. For a 3D location (h, w, d) , the mask prompt area is

$$\mathbf{M}_i^{(h,w,d)} = \begin{cases} 0 & \mathbf{A}_i^{(h,w,d)} > 0.5, \\ -\infty & \mathbf{A}_i^{(h,w,d)} \leq 0.5. \end{cases} \quad (15)$$

The mask prompt \mathbf{M}_i signifies the regions within the input 3D volume that pertain to an anomalous unseen category and an in-distribution seen organ class, respectively. These mask prompts, dynamically derived from the multi-scale feature embedding space, are instrumental in guiding tumor queries to concentrate on anomalous background features and acquire proficient representations for identifying unseen tumors effectively.

4.2.2. Diffusion-guided Query Refinement

Inspired by the diffusion process given in Equation (7), for multi-scale feature maps \mathbf{F}_i , the semantic diffusion process can be described as:

$$\frac{\partial \mathbf{F}_i}{\partial t} = \text{Div}(g(|\mathbf{D}_i|^2) \nabla \mathbf{F}_i), \quad (16)$$

where \mathbf{D}_i represents the guidance feature map with the same resolution as \mathbf{F}_i , and t refers to the time steps to enhance the

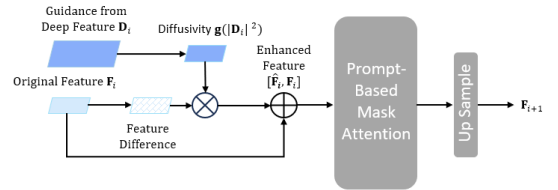


Figure 3: Diffusion-guided feature fusion mechanism.

guidance matrix, which in our context is $t = 1$. The diffusivity term $g(|\mathbf{D}_i|^2)$ is a monotonically decreasing function of the square of the gradient. In this context, diffusion near semantic boundary regions is dampened, while diffusion away from these boundaries is expedited. Therefore, it is imperative that \mathbf{D}_i encapsulates sufficient semantic information, enabling $g(|\mathbf{D}_i|^2)$ to serve as a reliable indicator of semantic boundaries for formulating the diffusivity.

We employ a diffusion-guided feature fusion mechanism to comprehensively enhance the boundaries. Given a feature map \mathbf{F}_i , the semantic guidance from the deep feature map $\hat{\mathbf{F}}_i$ is introduced to refine the original differential feature, resulting in an enhanced feature map. The partial differential equation governing the non-linear diffusion process can be approximately solved as [47]:

$$\hat{\mathbf{F}}_i[p] = \sum_{\tilde{p} \in \delta_p} g(|\mathbf{D}_i[\tilde{p}] - \mathbf{D}_i[p]|^2) \cdot (\mathbf{F}_i[\tilde{p}] - \mathbf{F}_i[p]), \quad (17)$$

$$\mathbf{F}_{i+1}[p] = \text{Conv}(\mathbf{F}_i[p] + \hat{\mathbf{F}}_i[p]), \quad i = 1, \dots, 4, \quad (18)$$

where p represents the position of an entry in the feature map, and δ_p denotes the $3 \times 3 \times 3$ local region centered at p , $g(|\mathbf{D}_i[\tilde{p}] - \mathbf{D}_i[p]|^2)$ is a matrix quantifying the similarity between semantic guidance feature maps with learnable weights, and $(\mathbf{F}_i[\tilde{p}] - \mathbf{F}_i[p])$ computes the feature disparity between different positions. As shown in Figure 3, Equation (17) formulates a differentiable matrix $g(|\mathbf{D}_i|^2) = g(|\mathbf{D}_i[\tilde{p}] - \mathbf{D}_i[p]|^2)$ based on the input feature map \mathbf{F}_i , transitioning to the boundary-enhanced guidance $\hat{\mathbf{F}}_i$ for this layer. Subsequently, the guidance $\hat{\mathbf{F}}_i$ is fused with the original feature map \mathbf{F}_i to generate a boundary-enhanced feature, which is put into the prompt-based mask attention (see (19)) and then convolved to upsample for the next layer \mathbf{F}_{i+1} . By combining the differential feature map $g(|\mathbf{D}_i|^2)$ with the semantic guidance $\hat{\mathbf{F}}_i$, we derive the feature map $\hat{\mathbf{F}}_i$ with enhanced boundary details for this layer. As illustrated in Figure 2(c), the enhanced feature map then acts as the key and value in the prompt-based masked attention layer.

For the i -th block in the Diffusion-guided Query Refinement (DQR) decoder, the tumor queries are updated via interactions with enhanced feature $[\mathbf{F}_i, \hat{\mathbf{F}}_i]$ and mask prompts \mathbf{A}_i by

$$\hat{\mathbf{T}}_i = \mathbf{T}_i + \text{Softmax}(\mathbf{A}_i + \mathbf{Q}_i \mathbf{K}_i^T) \mathbf{V}_i, \quad (19)$$

where \mathbf{T}_i is the linear projection from \mathbf{T} for each decoder layer, $\mathbf{Q}_i \in \mathbb{R}^{N_T \times C_i}$ is transformed from tumor query embedding \mathbf{T}_i , and \mathbf{K}_i and \mathbf{V}_i are transformed from enhanced feature maps $[\mathbf{F}_i, \hat{\mathbf{F}}_i]$. We then concatenate organ and tumor queries and apply self-attention among them to encode their relationship, facilitating the adjustment of their representations to promote distinct semantic differentiation between organs and tumors. Ultimately, we utilize these updated queries to generate the corresponding mask proposals.

4.2.3. Class Prompt Alignment

It is common to use a prompt model like CLIP [19] for zero-shot classification on the masks generated in Stage 1. Introducing a set of fixed class prompts helps our model generalize to a broader range of unseen categories, enabling the detection and segmentation of unseen organs and tumors. We include CLIP for weakly-supervised cross-modal alignment, aligning visual output feature maps with the high-level semantics of textual knowledge.

By utilizing CLIP as a pretrained text encoder, we generate text embeddings $\{\mathbf{k}_i \in \mathbb{R}^C\}_{i=1}^{N_o+N_T}$ from class prompts such as ‘‘a computerized tomography of a {CLS}’’ for every query class, where ‘‘CLS’’ is a class name such as ‘‘Liver’’. Detailed CLIP text prompts are provided below:

- The ‘‘CLS’’ for 25 organs are [‘Spleen’, ‘Right Kidney’, ‘Left Kidney’, ‘Gall Bladder’, ‘Esophagus’, ‘Liver’, ‘Stomach’, ‘Aorta’, ‘Postcava’, ‘Portal Vein and Splenic Vein’, ‘Pancreas’, ‘Right Adrenal Gland’, ‘Left Adrenal Gland’, ‘Duodenum’, ‘Hepatic Vessel’, ‘Right Lung’, ‘Left Lung’, ‘Colon’, ‘Intestine’, ‘Rectum’, ‘Bladder’, ‘Prostate’, ‘Left Head of Femur’, ‘Right Head of Femur’, ‘Celiac Truck’].
- The ‘‘CLS’’ for 20 tumors are [‘Spleen Tumor’, ‘Kidney Tumor’, ‘Kidney Cyst’, ‘Gall Bladder Tumor’, ‘Esophagus

Tumor’, ‘Liver Tumor’, ‘Stomach Tumor’, ‘Aortic Tumor’, ‘Postcava Tumor Thrombus’, ‘Portal Vein Tumor Thrombus’, ‘Pancreas Tumor’, ‘Adrenal Tumor’, ‘Adrenal Cyst’, ‘Duodenal Tumor’, ‘Hepatic Vessel Tumor’, ‘Lung Tumor’, ‘Lung Cyst’, ‘Colon Tumor’, ‘Small Intestinal Neoplasm’, ‘Rectal Tumor’].

Unlike other models, we calculate the cosine similarity between the text embeddings rather than relying solely on the vision embedding. The predicted probability distribution for the i -th query is determined as:

$$p_i = \frac{\exp(\frac{1}{\tau} \zeta(\mathbf{k}_i, \mathbf{q}_i))}{\sum_{j=1}^{N_o+N_T} \exp(\frac{1}{\tau} \zeta(\mathbf{k}_j, \mathbf{q}_i))}, \quad (20)$$

where ζ is the cosine similarity function, τ is the temperature parameter (set to 0.01 in our study), and \mathbf{k}_i and \mathbf{q}_i are the i -th text embedding and projected query embedding, respectively. Note that $\{\mathbf{q}_i \in \mathbb{R}^C\}_{i=1}^{N_o+N_T}$ is the concatenation $[\hat{\mathbf{Q}}_4^T, \hat{\mathbf{T}}_4^T]$ after passing through a linear projection layer. During training, the similarities between matched query embedding and text embedding should be maximized.

4.2.4. Loss Functions

In Stage 2, ground-truth labels and mask proposals are generalized to $\mathbb{R}^{(N_o+N_T) \times HWD}$. By adopting the cosine similarity map, we reformulate BCE loss \mathcal{L}_{BCE} for semantic segmentation by replacing \mathbf{Y} with $\text{diag}(\mathbf{p})\mathbf{Y}$, where $\mathbf{p} = (p_1, \dots, p_{N_o+N_T})$ with p_i given in (20), and utilize the same Dice loss as used in Stage 1. Note that we apply the BCE loss to the cosine similarity map to enhance the knowledge alignment between our classes and the class embeddings derived from CLIP.

Datasets	#Scans	Query Type	Stage
BTCV [48]	20	Organ	Training Stages 1&2
CHAOS [49]	40	Organ	Training Stages 1&2
Pancreas-CT [50]	60	Organ	Training Stages 1&2
CT-ORG [51]	140	Organ	Training Stages 1&2
WORD [52]	150	Organ	Training Stages 1&2
AMOS22 [53]	280	Organ	Training Stages 1&2
TotalSegmentor [54]	998	Organ	Training Stages 1&2
AbdomenCT-1K [55]	1000	Organ	Training Stages 1&2
LiTS [56]	52	Organ & Tumor	Training Stage 2
KiTS [57]	120	Organ & Tumor	Training Stage 2
BTCV [48]	30	Organ	Testing
LiTS [56]	79	Organ & Tumor	Testing
KiTS [57]	180	Organ & Tumor	Testing
MSD CT Tasks [58]	773	Organ & Tumor	Inference

Table 1: Implementation details for all datasets used.

5. Experiments

5.1. Datasets

We use CT scans from 11 publicly available datasets, including only those images with publicly released labels. The number of scans used from each dataset is summarized in Table 1.

The data are split into training, testing, and inference sets as follows:

- **Training set (2,860 images):** In Stage 1, we use 8 public datasets (2,668 images) to train organ labels, including BTCV [48], CHAOS [49], Pancreas-CT [50], CT-ORG [51], WORD [52], AMOS22 [53], TotalSegmentor [54], and AbdomenCT-1K [55]. In Stage 2, LiTS [56] and KiTS [57] are added to the training set. Note that 40% of BTCV, LiTS, and KiTS images (192 images) are used for training.
- **Testing set (289 images):** The remaining 60% of BTCV, LiTS, and KiTS images are used for testing seen tumor types.
- **Inference set (773 images):** For inference on unseen tumor types, we use the MSD dataset [58], which includes various segmentation tasks for four unseen tumor types in CT scans.

5.2. Evaluation Metrics

We use the Dice Similarity Coefficient (DSC) [59] to evaluate organ and tumor segmentation performance. Additionally, we present the Area Under the Receiver Operating Characteristic curve (AUROC) and the False Positive Rate at a True Positive Rate of 0.95 (FPR₉₅) as metrics for OOD localization [60, 61], given the critical importance of reducing false positives in clinical settings. Higher DSC and AUROC values indicate better performance, while lower FPR₉₅ values are preferred.

5.3. Training Details

Our DSM is implemented in PyTorch and trained on four NVIDIA A100 GPUs. (1) Stage 1: We use the Swin UNETR network [62] as the backbone. DSM consists of four kMax-Mamba decoder layers (K_d) and four Diffusion-guided decoder layers, each processing image features with output strides of 32, 16, 8, and 4, respectively. We employ the AdamW optimizer with a warm-up cosine scheduler spanning 50 epochs. During training, the batch size is set to 2 per GPU, with a patch size of $96 \times 96 \times 96$. The initial learning rate is 10^{-4} , with a momentum of 0.9 and a weight decay of 10^{-5} for 500 epochs. To enhance generalization, we incorporate extensive on-the-fly data augmentation techniques, including random rotation and scaling, elastic deformation, additive brightness, and gamma scaling. We use 25 organ queries ($N_o = 25$) for 25 organs. (2) Stage 2: We utilize the pretrained model from Stage 1, while setting the initial learning rate to 4×10^{-4} . The DQR decoder consists of four blocks, with each attention layer comprising eight heads. We employ 20 tumor queries ($N_T = 20$) for tumors/disease categories. Other parameters are the same as in Stage 1.

5.4. Baseline Models

Addressing the tasks of recognizing unseen tumors and OOD detection presents significant challenges in medical image segmentation. Hence, our baseline selection focuses on models with zero-shot capabilities and OOD detection. For inference on unseen tumor types in MSD data, We benchmark our

DSM against (1) prominent OVSS methods, including ZegFormer [40], OpenSeg [63], OVSeg [17], FreeSeg [18] and ZePT [3]; (2) prompt-based methods specific to medical imaging, including SAMMed [38] and Universeg [39]; and (3) OOD detection methods, including SynthCP [61], SML [64], and MaxQuery [41]. To evaluate the ability in fully-supervised training, we compare our DSM against medical image segmentation models, including nnUNet [8], the Universal model [2], Swin UNETR [62], and ZePT [3] on testing and inference datasets. We use the pretrained weights provided by the baseline models, except for Swin UNETR and ZePT, which are fine-tuned on the inference dataset since they were not originally pretrained on this data.

6. Results

6.1. Unseen Tumor Segmentation on MSD Data

We evaluate DSM on unseen tumors, with results summarized in Table 2. Across four unseen tumor categories from MSD, our DSM achieves the best performance in 8 out of 12 evaluation terms, and ranks second in remaining 4 with results comparable to the top scores.

Compared to the SOTA OVSS methods, DSM excels in AUROC and FPR₉₅ metrics for lung, pancreatic, and colorectal tumors, underscoring its superior performance in localizing unseen tumors. These results highlight that the proposed diffusion-guided boundary enhancement and multiple prompting mechanisms effectively link visual features to query embeddings, ultimately enhancing the model’s capability to localize unseen tumors.

In comparison to SAMMed and Universeg, two prompt-based models designed for medical image segmentation, our DSM consistently outperforms both across all tumor categories and evaluation metrics, highlighting its strong generalizability for unseen tumor segmentation. While UniverSeg significantly improves upon SAMMed, particularly in AUROC, it still lags behind DSM in segmenting less represented tumor types.

Relative to SOTA OOD detection methods, DSM surpasses the best-performing baseline, MaxQuery, across four tasks by at least 11.81% in FPR₉₅ and 9.26% in DSC. Unlike most OOD region segmentation methods that solely exploit visual modality information, DSM aligns visual features with linguistic semantics for cross-modal interaction. The results suggest that combining image features with medical domain knowledge enhances the semantic understanding of unseen tumors.

Figure 4 visualizes segmentation results on the MSD dataset from DSM and those baseline methods, where DSM demonstrates the best segmentation performance.

6.2. Segmentation of Seen Organs and Tumors on Testing Data

We evaluate the segmentation performance of DSM on familiar organs using the testing data and compare it with the four baselines (nnUNet, the Universal model, Swin UNETR, and ZePT). Table 3 shows that DSM outperforms all other methods, with an average improvement of at least 1.15% in DSC for BTCV, 1.07% for liver tumors in LiTS, and 0.89% for kidney

Method	Pancreas Tumor			Lung Tumor			Hepatic Vessel Tumor			Colon Tumor		
	AUROC↑	FPR ₉₅ ↓	DSC↑	AUROC↑	FPR ₉₅ ↓	DSC↑	AUROC↑	FPR ₉₅ ↓	DSC↑	AUROC↑	FPR ₉₅ ↓	DSC↑
ZegFormer [40]	66.45±1.14	69.33±1.28	14.92±0.76	41.31±0.36	81.78±4.33	9.94±0.49	75.39±0.59	55.94±0.60	30.81±0.70	50.13±0.07	78.81±0.07	11.34±0.16
OpenSeg [63]	44.56±1.34	85.19±0.91	10.05±0.34	23.49±0.72	91.75±6.31	6.12±0.59	59.23±0.57	70.52±0.52	23.38±0.79	41.76±0.10	89.44±0.05	7.13±0.15
OVSeg [17]	70.22±0.71	59.73±1.05	19.36±0.43	52.93±0.46	68.65±0.53	14.11±0.55	85.77±0.37	40.28±0.72	35.66±0.55	59.94±0.07	65.25±0.08	15.76±0.14
FreeSeg [18]	69.98±0.75	60.75±0.96	18.19±0.44	49.92±0.32	70.39±0.43	13.26±0.43	85.62±0.44	40.77±0.88	35.08±0.31	56.45±0.05	68.49±0.04	14.71±0.13
ZePT [3]	86.81±0.65	35.18±0.82	37.67±0.29	77.84±0.32	44.30±1.02	27.22±0.21	91.57±0.27	20.64±0.24	52.94±0.27	82.36±0.04	40.73±0.03	30.45±0.05
SAMMed [38]	72.75±1.24	57.84±1.43	22.43±0.23	64.28±0.28	48.27±2.99	17.97±0.23	78.88±0.44	56.65±0.66	35.11±0.21	61.47±0.14	63.55±0.05	16.46±0.11
UniverseSeg [39]	79.64±1.05	40.49±1.01	32.51±0.50	67.22±0.37	48.19±1.21	23.38±0.12	87.57±0.31	38.22±0.93	35.25±0.44	79.29±0.09	45.51±0.03	28.72±0.05
SynthCP [61]	51.24±1.42	81.69±1.45	11.33±0.25	25.85±0.41	90.28±5.13	6.43±0.32	70.12±0.56	63.55±0.73	28.01±0.56	43.84±0.15	87.71±0.07	8.74±0.07
SML [64]	37.95±1.90	89.93±1.15	9.72±0.18	20.18±0.39	93.65±4.91	6.02±0.39	57.44±0.68	70.96±0.65	22.97±0.52	22.41±0.11	92.07±0.15	6.65±0.09
MaxQuery [41]	68.99±1.03	59.93±1.11	18.15±0.70	48.24±0.57	70.47±4.40	11.29±0.32	83.66±0.45	42.45±0.81	34.30±0.51	50.47±0.09	69.88±0.03	13.43±0.05
DSM	88.61±0.65	30.04±0.81	38.86±0.26	76.91±0.35	43.72±1.01	28.65±0.32	89.45±0.26	34.64±0.24	43.56±0.26	83.34±0.04	41.78±0.04	31.52±0.05

Table 2: Segmentation performance of unseen tumors on MSD dataset. All scores (mean ± SE) are in %.

Method	BTCV			LiTS			KiTS		
	AUROC↑	FPR ₉₅ ↓	DSC↑	AUROC↑	FPR ₉₅ ↓	DSC↑	AUROC↑	FPR ₉₅ ↓	DSC↑
nnUNet [8]	88.07 ± 0.17	24.85 ± 0.15	82.23 ± 0.30	91.21 ± 0.12	21.03±0.15	77.15 ± 0.30	93.35±0.10	18.76±0.11	85.18 ± 0.09
Universal [2]	94.10 ± 0.15	19.77 ± 0.11	86.38 ± 0.23	92.88 ± 0.09	19.72±0.12	80.58 ± 0.26	95.06±0.06	16.18±0.07	87.05 ± 0.08
Swin UNETR [62]	90.01 ± 0.16	21.31 ± 0.14	82.26 ± 0.29	90.01 ± 0.12	21.11±0.14	76.79 ± 0.31	94.45±0.10	18.22±0.10	85.52 ± 0.08
ZePT [3]	96.75 ± 0.12	17.04 ± 0.06	87.09 ± 0.22	93.03 ± 0.08	18.07±0.09	81.66 ± 0.24	95.97±0.06	15.07±0.05	87.73 ± 0.07
DSM	96.87 ± 0.11	16.88 ± 0.06	88.24 ± 0.21	93.24±0.08	18.56±0.11	82.73 ± 0.24	96.02±0.05	14.98±0.05	88.62 ± 0.07

Table 3: Segmentation results for 13 organs in BTCV, liver tumor in LiTS, and kidney tumor in KiTS. All scores (mean ± SE) are in %.

tumors in KiTS. Notably, the Universal model [2] and ZePT [3] adopt a CLIP text encoder and design an architecture for query refinement but use the original visual features. DSM takes one step further by designing a diffusion-guided boundary enhancement structure on visual features to improve the semantic segmentation. These improvements demonstrate that DSM can also segment seen organs and tumors with high accuracy.

6.3. Fully Supervised Segmentation on MSD Data

To evaluate the fully supervised performance of DSM on the MSD dataset, we fine-tune it on this dataset and compare it with the other four SOTA segmentation models. The MSD dataset we used, consisting of 773 CT scans for Lung, Colon, Hepatic Vessel, and Pancreas, is split into 652 images for training and 121 for testing. We apply the same data split to fine-tune Swin UNETR and ZePT. For nnUNet and the Universal model, which were pretrained on the MSD dataset, we use their pretrained models directly for comparison. The results are presented in Table 4. Our DSM achieves the best performance in 7 out of 12 evaluation terms. In the remaining 5, it ranks second, with results that are comparable to the best.

Figure 5 shows the qualitative results on DSM with medical segmentation models and highlights the advantages of DSM. Most competing methods suffer from incomplete segmentation of the target and misclassification of background regions as tumors (false positives). In contrast, DSM produces sharper boundaries and generates results that are more consistent with the ground truth than all other models.

6.4. Ablation Studies

We conduct ablation studies to evaluate the effectiveness of four key components in our DSM framework, including the kMM block, the anomaly mask visual prompt attention

(AMVP), the DQR process, and the CLIP text embedding. The evaluation is performed on liver tumor segmentation in the LiTS dataset and colon tumor segmentation in the MSD dataset. Results summarized in Table 5 show that the full model incorporating all four components achieves the best performance.

Significance of kMM. Rows 2 and 6 of Table 5 compare the kMM blocks with the vanilla MaskFormer blocks for query updates with the Swin UNETR backbone. A modest performance improvement is observed with kMM on both the testing and inference sets, indicating that incorporating an SSM is beneficial for maintaining strong performance during long-sequence modeling tasks.

Efficiency of Mask Prompts in OOD. As shown in Rows 3 and 6 of Table 5, the AMVP is compared with a vanilla self-attention layer, directly concatenating multiple anomaly score maps with image features to update the advanced queries. Removing AMVP leads to a decline in performance for both seen and unseen tumors.

Importance of Diffusion-Guided Query Refinement. As depicted in Rows 4 and 6 of Table 5, the DQR process is compared with an alternative approach using a projection layer. The feature map undergoes processing through the projection layer and is fused with the upper layer feature map. The result in Table 5 suggests that feature fusion and boundary enhancement play a significant role in semantic segmentation tasks. Various methods introduce diffusion process into segmentation networks to enhance performance in diverse ways [14, 15], and we believe this is a general approach that can benefit deep learning models in various popular visual tasks.

Usage of CLIP text embedding. As shown in Rows 5 and 6 of Table 5, using the cosine similarity map with CLIP text embedding outperforms the approach of using the Hungarian matching algorithm, which is used in MaskFormer [25, 26] to

Method	Pancreas Tumor			Lung Tumor			Hepatic Vessel Tumor			Colon Tumor		
	AUROC \uparrow	FPR $_{95}\downarrow$	DSC \uparrow	AUROC \uparrow	FPR $_{95}\downarrow$	DSC \uparrow	AUROC \uparrow	FPR $_{95}\downarrow$	DSC \uparrow	AUROC \uparrow	FPR $_{95}\downarrow$	DSC \uparrow
nnUNet [8]	91.75 \pm 0.07	25.88 \pm 0.09	50.45 \pm 0.13	90.75 \pm 0.06	24.56 \pm 0.16	66.57 \pm 0.18	86.91 \pm 0.19	31.87 \pm 0.17	68.20 \pm 0.30	91.55 \pm 0.05	23.75 \pm 0.07	50.07 \pm 0.07
Universal [2]	93.32 \pm 0.05	19.12 \pm 0.06	60.83 \pm 0.10	94.53 \pm 0.04	18.85 \pm 0.14	67.11 \pm 0.15	89.24 \pm 0.15	30.77 \pm 0.15	69.47 \pm 0.24	93.15 \pm 0.05	19.24 \pm 0.05	62.15 \pm 0.06
Swin UNETR [62] (fine-tuned)	91.83 \pm 0.06	24.47 \pm 0.08	52.54 \pm 0.12	92.01 \pm 0.05	22.31 \pm 0.16	68.90 \pm 0.16	87.45 \pm 0.18	31.33 \pm 0.17	68.63 \pm 0.28	91.73 \pm 0.05	22.34 \pm 0.08	50.55 \pm 0.06
ZePT [3] (fine-tuned)	93.85 \pm 0.05	18.87 \pm 0.07	62.10 \pm 0.10	93.97 \pm 0.05	18.17 \pm 0.12	62.15 \pm 0.16	91.24\pm0.16	28.08\pm0.14	70.65\pm0.24	93.97\pm0.05	18.91 \pm 0.05	64.87\pm0.05
DSM (fine-tuned)	94.07\pm0.04	18.04\pm0.11	62.25\pm0.09	94.91\pm0.04	17.72\pm0.12	69.45\pm0.14	89.75 \pm 0.15	29.91 \pm 0.15	69.95 \pm 0.26	93.52 \pm 0.04	18.68\pm0.04	63.31 \pm 0.05

Table 4: Segmentation results for unseen tumors on MSD dataset. All scores (mean \pm SE) are in %.

Modules				Liver Tumor in LiTS (Seen)			Colon Tumor in MSD (Unseen)		
kMM	AMVP	DQR	CLIP	AUROC \uparrow	FPR $_{95}\downarrow$	DSC \uparrow	AUROC \uparrow	FPR $_{95}\downarrow$	DSC \uparrow
				90.92 \pm 0.14	23.18 \pm 0.15	78.98 \pm 0.28	78.22 \pm 0.05	45.82 \pm 0.08	25.07 \pm 0.07
	\checkmark	\checkmark	\checkmark	92.23 \pm 0.13	21.47 \pm 0.15	80.22 \pm 0.26	79.18 \pm 0.05	43.77 \pm 0.07	27.31 \pm 0.07
\checkmark		\checkmark	\checkmark	93.14 \pm 0.11	21.11 \pm 0.13	81.16 \pm 0.27	79.03 \pm 0.05	42.64 \pm 0.05	26.84 \pm 0.06
\checkmark	\checkmark		\checkmark	92.73 \pm 0.09	19.41 \pm 0.12	80.84 \pm 0.25	80.64 \pm 0.04	43.75 \pm 0.05	29.03 \pm 0.06
\checkmark	\checkmark	\checkmark		91.73 \pm 0.11	20.03 \pm 0.13	80.65 \pm 0.27	79.32 \pm 0.05	43.45 \pm 0.08	29.76 \pm 0.07
\checkmark	\checkmark	\checkmark	\checkmark	93.24\pm0.08	18.56\pm0.11	82.73\pm0.24	83.34\pm0.04	41.78\pm0.04	31.52\pm0.05

Table 5: Ablation study of DSM’s different components on LiTS and MSD datasets. All scores (mean \pm SE) are in %.

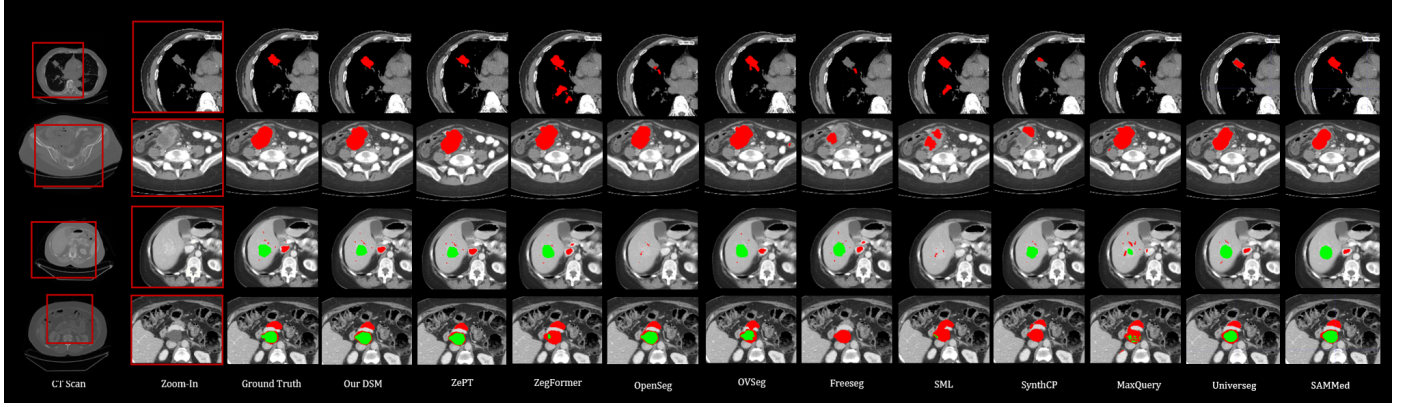


Figure 4: Qualitative visualization of the proposed DSM compared with competing models in unseen tumor segmentation on MSD dataset. The segmentation results shown from Rows 1 to 4 correspond to Lung Tumor, Colon Tumor, Hepatic Vessel Tumor, and Pancreas Tumor, respectively. In Rows 1 and 2, the red region represents the tumor area, while in Rows 3 and 4, the red region represents the organ and the green region represents the tumor.

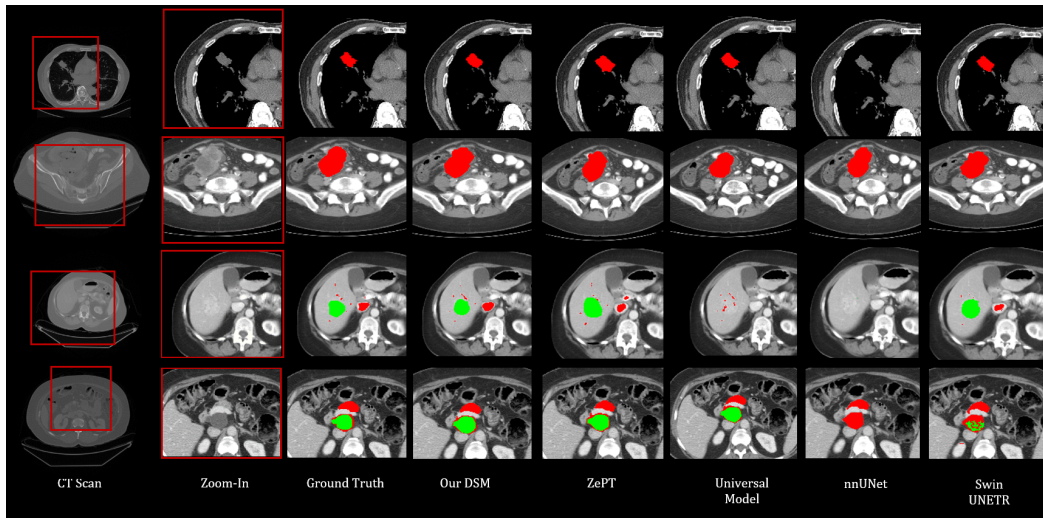


Figure 5: Qualitative visualization of the proposed DSM compared with competing models in fully supervised segmentation on MSD dataset. The segmentation results shown from Rows 1 to 4 correspond to Lung Tumor, Colon Tumor, Hepatic Vessel Tumor, and Pancreas Tumor, respectively. In Rows 1 and 2, the red region represents the tumor area, while in Rows 3 and 4, the red region represents the organ and the green region represents the tumor.

match queries with mask proposals.

Model without the 4 Components. Row 1 of Table 5 shows the result for the model in which all the four components are replaced by cross-attention layers. This model demonstrates the poorest performance among all the models presented in Table 5.

7. Conclusion

We propose DSM, a pioneering segmentation framework that leverages query refinement and visual boundary enhancement for precise semantic organ segmentation and tumor detection. A key innovation is the incorporation of kMM layers to bolster long-term memory within query embeddings. We also introduce a mask visual prompt to prioritize tumor detection and utilize the diffusion-guided query decoder for refined tumor boundary enhancement. Furthermore, we enhance the model’s robustness by conducting cosine similarity alignment between class and text embeddings. The substantial performance improvements observed with DSM across multiple organ and tumor segmentation tasks underscore its efficacy.

Acknowledgements

This research was partially supported by Dr. Hai Shu’s NYU GPH Research Support Grant. This work was supported in part through the NYU IT High Performance Computing resources, services, and staff expertise.

References

- [1] S. Zhang, D. Metaxas, On the challenges and perspectives of foundation models for medical image analysis, *Medical Image Analysis* (2023) 102996.
- [2] J. Liu, Y. Zhang, J.-N. Chen, J. Xiao, Y. Lu, B. A. Landman, Y. Yuan, A. Yuille, Y. Tang, Z. Zhou, Clip-driven universal model for organ segmentation and tumor detection, in: *Proceedings of the IEEE/CVF International Conference on Computer Vision*, 2023, pp. 21152–21164.
- [3] Y. Jiang, Z. Huang, R. Zhang, X. Zhang, S. Zhang, Zept: Zero-shot pan-tumor segmentation via query-disentangling and self-prompting, in: *Proceedings of the IEEE/CVF Conference on Computer Vision and Pattern Recognition*, 2024, pp. 11386–11397.
- [4] A. Gu, K. Goel, C. Ré, Efficiently modeling long sequences with structured state spaces, *arXiv preprint arXiv:2111.00396* (2021).
- [5] A. Gu, T. Dao, Mamba: Linear-time sequence modeling with selective state spaces, *arXiv preprint arXiv:2312.00752* (2023).
- [6] J. D. Hamilton, State-space models, *Handbook of econometrics* 4 (1994) 3039–3080.
- [7] J. Ma, F. Li, B. Wang, U-mamba: Enhancing long-range dependency for biomedical image segmentation, *arXiv preprint arXiv:2401.04722* (2024).
- [8] F. Isensee, P. F. Jaeger, S. A. Kohl, J. Petersen, K. H. Maier-Hein, nnu-net: a self-configuring method for deep learning-based biomedical image segmentation, *Nature methods* 18 (2) (2021) 203–211.
- [9] L. Zhu, B. Liao, Q. Zhang, X. Wang, W. Liu, X. Wang, Vision mamba: Efficient visual representation learning with bidirectional state space model, *arXiv preprint arXiv:2401.09417* (2024).
- [10] T. Dao, A. Gu, Transformers are ssms: Generalized models and efficient algorithms through structured state space duality, *arXiv preprint arXiv:2405.21060* (2024).
- [11] A. Vaswani, N. Shazeer, N. Parmar, J. Uszkoreit, L. Jones, A. N. Gomez, Ł. Kaiser, I. Polosukhin, Attention is all you need, *Advances in neural information processing systems* 30 (2017).
- [12] W. Peebles, S. Xie, Scalable diffusion models with transformers, in: *Proceedings of the IEEE/CVF International Conference on Computer Vision*, 2023, pp. 4195–4205.
- [13] J. Wu, R. Fu, H. Fang, Y. Zhang, Y. Yang, H. Xiong, H. Liu, Y. Xu, Med-segdiff: Medical image segmentation with diffusion probabilistic model, in: *Medical Imaging with Deep Learning*, PMLR, 2024, pp. 1623–1639.
- [14] H. Wang, J. Cao, R. M. Anwer, J. Xie, F. S. Khan, Y. Pang, Dformer: Diffusion-guided transformer for universal image segmentation, *arXiv preprint arXiv:2306.03437* (2023).
- [15] H. Tan, S. Wu, J. Pi, Semantic diffusion network for semantic segmentation, *Advances in Neural Information Processing Systems* 35 (2022) 8702–8716.
- [16] J. Zhang, C. Herrmann, J. Hur, L. Polania Cabrera, V. Jampani, D. Sun, M.-H. Yang, A tale of two features: Stable diffusion complements dino for zero-shot semantic correspondence, *Advances in Neural Information Processing Systems* 36 (2024).
- [17] F. Liang, B. Wu, X. Dai, K. Li, Y. Zhao, H. Zhang, P. Zhang, P. Vajda, D. Marculescu, Open-vocabulary semantic segmentation with mask-adapted clip, in: *Proceedings of the IEEE/CVF Conference on Computer Vision and Pattern Recognition*, 2023, pp. 7061–7070.
- [18] J. Qin, J. Wu, P. Yan, M. Li, R. Yuxi, X. Xiao, Y. Wang, R. Wang, S. Wen, X. Pan, et al., Freeseg: Unified, universal and open-vocabulary image segmentation, in: *Proceedings of the IEEE/CVF Conference on Computer Vision and Pattern Recognition*, 2023, pp. 19446–19455.
- [19] A. Radford, J. W. Kim, C. Hallacy, A. Ramesh, G. Goh, S. Agarwal, G. Sastry, A. Askell, P. Mishkin, J. Clark, et al., Learning transferable visual models from natural language supervision, in: *International conference on machine learning*, PMLR, 2021, pp. 8748–8763.
- [20] J. Devlin, M.-W. Chang, K. Lee, K. Toutanova, Bert: Pre-training of deep bidirectional transformers for language understanding, *arXiv preprint arXiv:1810.04805* (2018).
- [21] A. Joulin, E. Grave, P. Bojanowski, T. Mikolov, Bag of tricks for efficient text classification, *arXiv preprint arXiv:1607.01759* (2016).
- [22] A. Zareian, K. D. Rosa, D. H. Hu, S.-F. Chang, Open-vocabulary object detection using captions, in: *Proceedings of the IEEE/CVF Conference on Computer Vision and Pattern Recognition*, 2021, pp. 14393–14402.
- [23] D. Huynh, J. Kuen, Z. Lin, J. Gu, E. Elhamifar, Open-vocabulary instance segmentation via robust cross-modal pseudo-labeling, in: *Proceedings of the IEEE/CVF Conference on Computer Vision and Pattern Recognition*, 2022, pp. 7020–7031.
- [24] Y. Rao, W. Zhao, G. Chen, Y. Tang, Z. Zhu, G. Huang, J. Zhou, J. Lu, Denseclip: Language-guided dense prediction with context-aware prompting, in: *Proceedings of the IEEE/CVF conference on computer vision and pattern recognition*, 2022, pp. 18082–18091.
- [25] B. Cheng, A. Schwing, A. Kirillov, Per-pixel classification is not all you need for semantic segmentation, *Advances in neural information processing systems* 34 (2021) 17864–17875.
- [26] B. Cheng, I. Misra, A. G. Schwing, A. Kirillov, R. Girdhar, Masked-attention mask transformer for universal image segmentation, in: *Proceedings of the IEEE/CVF conference on computer vision and pattern recognition*, 2022, pp. 1290–1299.
- [27] X. Fang, P. Yan, Multi-organ segmentation over partially labeled datasets with multi-scale feature abstraction, *IEEE Transactions on Medical Imaging* 39 (11) (2020) 3619–3629.
- [28] Y. Tang, D. Yang, W. Li, H. R. Roth, B. Landman, D. Xu, V. Nath, A. Hatamizadeh, Self-supervised pre-training of swin transformers for 3d medical image analysis, in: *Proceedings of the IEEE/CVF conference on computer vision and pattern recognition*, 2022, pp. 20730–20740.
- [29] A. Kirillov, E. Mintun, N. Ravi, H. Mao, C. Rolland, L. Gustafson, T. Xiao, S. Whitehead, A. C. Berg, W.-Y. Lo, et al., Segment anything, in: *Proceedings of the IEEE/CVF International Conference on Computer Vision*, 2023, pp. 4015–4026.
- [30] C. Chen, J. Miao, D. Wu, Z. Yan, S. Kim, J. Hu, A. Zhong, Z. Liu, L. Sun, X. Li, et al., Ma-sam: Modality-agnostic sam adaptation for 3d medical image segmentation, *arXiv preprint arXiv:2309.08842* (2023).
- [31] Z. Gu, S. Zhou, L. Niu, Z. Zhao, L. Zhang, Context-aware feature generation for zero-shot semantic segmentation, in: *Proceedings of the 28th ACM International Conference on Multimedia*, 2020, pp. 1921–1929.
- [32] M. Moor, O. Banerjee, Z. S. H. Abad, H. M. Krumholz, J. Leskovec, E. J. Topol, P. Rajpurkar, Foundation models for generalist medical artificial intelligence, *Nature* 616 (7956) (2023) 259–265.

- [33] T. Brown, B. Mann, N. Ryder, M. Subbiah, J. D. Kaplan, P. Dhariwal, A. Neelakantan, P. Shyam, G. Sastry, A. Askell, et al., Language models are few-shot learners, *Advances in neural information processing systems* 33 (2020) 1877–1901.
- [34] K. Singhal, S. Azizi, T. Tu, S. S. Mahdavi, J. Wei, H. W. Chung, N. Scales, A. Tanwani, H. Cole-Lewis, S. Pföhl, et al., Large language models encode clinical knowledge, *Nature* 620 (7972) (2023) 172–180.
- [35] B. Li, K. Q. Weinberger, S. Belongie, V. Koltun, R. Ranftl, Language-driven semantic segmentation, *arXiv preprint arXiv:2201.03546* (2022).
- [36] Z. Wang, Y. Lu, Q. Li, X. Tao, Y. Guo, M. Gong, T. Liu, Cris: Clip-driven referring image segmentation, in: *Proceedings of the IEEE/CVF conference on computer vision and pattern recognition*, 2022, pp. 11686–11695.
- [37] K. Park, S. Woo, S. W. Oh, I. S. Kweon, J.-Y. Lee, Per-clip video object segmentation, in: *Proceedings of the IEEE/CVF Conference on Computer Vision and Pattern Recognition*, 2022, pp. 1352–1361.
- [38] H. Wang, S. Guo, J. Ye, Z. Deng, J. Cheng, T. Li, J. Chen, Y. Su, Z. Huang, Y. Shen, et al., Sam-med3d: towards general-purpose segmentation models for volumetric medical images, in: *European Conference on Computer Vision*, Springer, 2025, pp. 51–67.
- [39] V. I. Butoi, J. J. G. Ortiz, T. Ma, M. R. Sabuncu, J. Guttag, A. V. Dalca, Universeg: Universal medical image segmentation, in: *Proceedings of the IEEE/CVF International Conference on Computer Vision*, 2023, pp. 21438–21451.
- [40] J. Ding, N. Xue, G.-S. Xia, D. Dai, Decoupling zero-shot semantic segmentation, in: *Proceedings of the IEEE/CVF Conference on Computer Vision and Pattern Recognition*, 2022, pp. 11583–11592.
- [41] M. Yuan, Y. Xia, H. Dong, Z. Chen, J. Yao, M. Qiu, K. Yan, X. Yin, Y. Shi, X. Chen, et al., Devil is in the queries: advancing mask transformers for real-world medical image segmentation and out-of-distribution localization, in: *Proceedings of the IEEE/CVF Conference on Computer Vision and Pattern Recognition*, 2023, pp. 23879–23889.
- [42] P. Perona, J. Malik, Scale-space and edge detection using anisotropic diffusion, *IEEE Transactions on pattern analysis and machine intelligence* 12 (7) (1990) 629–639.
- [43] K. He, X. Zhang, S. Ren, J. Sun, Deep residual learning for image recognition, in: *Proceedings of the IEEE conference on computer vision and pattern recognition*, 2016, pp. 770–778.
- [44] Z. Liu, Y. Lin, Y. Cao, H. Hu, Y. Wei, Z. Zhang, S. Lin, B. Guo, Swin transformer: Hierarchical vision transformer using shifted windows, in: *Proceedings of the IEEE/CVF international conference on computer vision*, 2021, pp. 10012–10022.
- [45] Q. Yu, H. Wang, S. Qiao, M. Collins, Y. Zhu, H. Adam, A. Yuille, L.-C. Chen, k-means mask transformer, in: *European Conference on Computer Vision*, Springer, 2022, pp. 288–307.
- [46] S. Elfwing, E. Uchibe, K. Doya, Sigmoid-weighted linear units for neural network function approximation in reinforcement learning, *Neural networks* 107 (2018) 3–11.
- [47] G. Sapiro, *Geometric partial differential equations and image analysis*, Cambridge university press, 2006.
- [48] B. Landman, Z. Xu, J. Igelsias, M. Styner, T. Langerak, A. Klein, Miccai multi-atlas labeling beyond the cranial vault—workshop and challenge, in: *Proc. MICCAI Multi-Atlas Labeling Beyond Cranial Vault—Workshop Challenge*, Vol. 5, 2015, p. 12.
- [49] A. E. Kavur, N. S. Gezer, M. Barış, S. Aslan, P.-H. Conze, V. Groza, D. D. Pham, S. Chatterjee, P. Ernst, S. Özkan, et al., Chaos challenge-combined (ct-mr) healthy abdominal organ segmentation, *Medical Image Analysis* 69 (2021) 101950.
- [50] H. R. Roth, L. Lu, A. Farag, H.-C. Shin, J. Liu, E. B. Turkbey, R. M. Summers, Deeporgan: Multi-level deep convolutional networks for automated pancreas segmentation, in: *Medical Image Computing and Computer-Assisted Intervention—MICCAI 2015: 18th International Conference*, Munich, Germany, October 5–9, 2015, *Proceedings, Part I* 18, Springer, 2015, pp. 556–564.
- [51] B. Rister, D. Yi, K. Shivakumar, T. Nobashi, D. L. Rubin, Ct-org, a new dataset for multiple organ segmentation in computed tomography, *Scientific Data* 7 (1) (2020) 381.
- [52] X. Luo, W. Liao, J. Xiao, J. Chen, T. Song, X. Zhang, K. Li, D. N. Metaxas, G. Wang, S. Zhang, Word: A large scale dataset, benchmark and clinical applicable study for abdominal organ segmentation from ct image, *arXiv preprint arXiv:2111.02403* (2021).
- [53] Y. Ji, H. Bai, C. Ge, J. Yang, Y. Zhu, R. Zhang, Z. Li, L. Zhanng, W. Ma, X. Wan, et al., Amos: A large-scale abdominal multi-organ benchmark for versatile medical image segmentation, *Advances in Neural Information Processing Systems* 35 (2022) 36722–36732.
- [54] J. Wasserthal, H.-C. Breit, M. T. Meyer, M. Pradella, D. Hinck, A. W. Sauter, T. Heye, D. T. Boll, J. Cyriac, S. Yang, et al., Totalsegmentator: Robust segmentation of 104 anatomic structures in ct images, *Radiology: Artificial Intelligence* 5 (5) (2023).
- [55] J. Ma, Y. Zhang, S. Gu, C. Zhu, C. Ge, Y. Zhang, X. An, C. Wang, Q. Wang, X. Liu, et al., Abdomenct-1k: Is abdominal organ segmentation a solved problem?, *IEEE Transactions on Pattern Analysis and Machine Intelligence* 44 (10) (2021) 6695–6714.
- [56] P. Bilic, P. Christ, H. B. Li, E. Vorontsov, A. Ben-Cohen, G. Kaissis, A. Szeskin, C. Jacobs, G. E. H. Mamani, G. Chartrand, et al., The liver tumor segmentation benchmark (lits), *Medical Image Analysis* 84 (2023) 102680.
- [57] N. Heller, S. McSweeney, M. T. Peterson, S. Peterson, J. Rickman, B. Stai, R. Tejpaul, M. Oestreich, P. Blake, J. Rosenberg, et al., An international challenge to use artificial intelligence to define the state-of-the-art in kidney and kidney tumor segmentation in ct imaging. (2020).
- [58] M. Antonelli, A. Reinke, S. Bakas, K. Farahani, A. Kopp-Schneider, B. A. Landman, G. Litjens, B. Menze, O. Ronneberger, R. M. Summers, et al., The medical segmentation decathlon, *Nature communications* 13 (1) (2022) 4128.
- [59] A. A. Taha, A. Hanbury, Metrics for evaluating 3d medical image segmentation: analysis, selection, and tool, *BMC medical imaging* 15 (2015) 1–28.
- [60] Q. Wu, Y. Chen, C. Yang, J. Yan, Energy-based out-of-distribution detection for graph neural networks, *arXiv preprint arXiv:2302.02914* (2023).
- [61] Y. Xia, Y. Zhang, F. Liu, W. Shen, A. L. Yuille, Synthesize then compare: Detecting failures and anomalies for semantic segmentation, in: *Computer Vision—ECCV 2020: 16th European Conference*, Glasgow, UK, August 23–28, 2020, *Proceedings, Part I* 16, Springer, 2020, pp. 145–161.
- [62] A. Hatamizadeh, V. Nath, Y. Tang, D. Yang, H. R. Roth, D. Xu, Swin unetr: Swin transformers for semantic segmentation of brain tumors in mri images, in: *International MICCAI brainlesion workshop*, Springer, 2021, pp. 272–284.
- [63] G. Ghiasi, X. Gu, Y. Cui, T.-Y. Lin, Scaling open-vocabulary image segmentation with image-level labels, in: *European Conference on Computer Vision*, Springer, 2022, pp. 540–557.
- [64] S. Jung, J. Lee, D. Gwak, S. Choi, J. Choo, Standardized max logits: A simple yet effective approach for identifying unexpected road obstacles in urban-scene segmentation, in: *Proceedings of the IEEE/CVF International Conference on Computer Vision*, 2021, pp. 15425–15434.